Journal of Oceanology and Limnology

https://doi.org/10.1007/s00343-026-5517-6

Research Paper

Residual-enhanced broad learning system: a fusion framework for multi-class ocean phenomena recognition in SAR imagery*

Jianing SHAO[1, 2], Sheng WANG[1, **], Guihong LIU[1], Wentao MA[1], Yang YU[1], Tianjie ZHAO[1], Xiaofeng YANG[3]

[1] *State Key Laboratory of Remote Sensing and Digital Earth, Aerospace Information Research Institute, Chinese Academy of Sciences, Beijing 100101, China*

[2] *University of Chinese Academy of Sciences, Beijing 100049, China*

[3] *Institute of Space Earth Science, Nanjing University, Suzhou 215163, China*

Received Dec. 18, 2025; accepted in principle Apr. 2, 2026; accepted for publication May 18, 2026

© Chinese Society for Oceanology and Limnology, Science Press and Springer-Verlag GmbH Germany, part of Springer Nature 2026

Abstract Accurate and efficient classification of oceanic phenomena is crucial for marine environmental monitoring, particularly given the rapid growth of remote sensing data. However, conventional deep learning methods often suffer from high training costs and lack flexibility in rapidly updating their parameters. To address these challenges, this study proposes a Residual-Enhanced Broad Learning System (RE-BLS) for efficient classification of ocean phenomena using synthetic aperture radar (SAR) images. RE-BLS combines a pre-trained ResNet-50 for deep feature extraction with a broad learning system (BLS) for fast and lightweight classification. The model is trained and evaluated on the TenGeoP-SARwv dataset, which contains wave-mode SAR images labeled with ten representative oceanic phenomena. Experimental results show that RE-BLS achieves an overall classification accuracy of 98.48%, significantly outperforming the original BLS model, which attains only 56.07%. Furthermore, RE-BLS requires approximately only 1/50 of the training time of the deep conventional neural network ResNet-50, while achieving comparable accuracy. In addition, its incremental learning capability is validated by progressively introducing new training data. Overall, RE-BLS demonstrates strong potential for large-scale and temporally dynamic remote sensing applications due to its high computational efficiency and adaptability.

Keyword: synthetic aperture radar (SAR); ocean phenomena recognition; broad learning system (BLS); feature extraction; residual module

1 INTRODUCTION

The identification and monitoring of key oceanic elements, such as wind, waves, and currents, as well as oceanic phenomena including internal waves, ocean fronts, tropical cyclones, and rain cells, are critical to understanding the marine environment, managing ocean resources, and studying climate change (Bojinski et al., 2014). In recent decades, satellite remote sensing has become the dominant approach for acquiring ocean data, driven by rapid developments in sensor technologies, particularly in operating wavelengths, swath width, and spatiotemporal resolution. Among various remote sensing instruments, synthetic aperture radar (SAR) stands out for its ability to provide high-resolution imagery under all-weather and all-day conditions. By capturing the detailed structural and textural features of the sea surface, SAR provides essential information for analyzing ocean dynamics and associated physical processes.

The advancement of SAR satellite technology

* Supported by the National Key R&D Program of China (No. 2023YFB3907700)

Academic Papers of the 28th Annual Meeting of the China Association for Science and Technology

** Corresponding author: wangsheng01@aircas.ac.cn

has led to a rapid increase in the observational data. For example, the Sentinel-1 satellite acquires nearly 60 000 VV-polarized wave mode vignettes over the ocean surface each month (Wang et al., 2019). These SAR images have been used for monitoring oceanic phenomena and retrieving geophysical parameters, including mesoscale eddy detection and feature analysis (Duo et al., 2019; Zi et al., 2024), internal wave observation and inversion (Vasavi et al., 2021; Zhang et al., 2022a), and ocean front identification (Sun et al., 2022; Xu et al., 2022), highlighting their practical value for mesoscale oceanic phenomena studies. However, despite the rapid growth of observational data, the effective utilization rate of SAR data remains relatively low, and a large proportion of the acquired data has not been fully explored or exploited (Liu et al., 2017a). In particular, the recognition of small-scale oceanic phenomena, such as rain cells associated with heavy precipitation, floating sea ice, and micro convective cells, has received relatively little attention. With the continuous accumulation of ocean remote sensing data, the development of efficient and accurate methods for oceanic phenomena detection and classification has become increasingly urgent, as it is essential for achieving more comprehensive ocean monitoring and data utilization.

Traditional manual interpretation of SAR imagery is no longer sufficient to handle the rapidly growing volume of remote sensing data. Recent advances in machine learning and deep learning have substantially improved the automation of oceanic phenomena recognition and classification. A variety of deep learning algorithms have been applied to tasks such as sea ice classification (Li et al., 2021b; Huang et al., 2024; Rogers et al., 2024), oil spill detection (Xu et al., 2014; Temitope Yekeen et al., 2020), oceanic eddy identification (Sun et al., 2021; Huang et al., 2022; Santana et al., 2022), and ocean artificial target detection (He et al., 2021; Yang et al., 2022). Among these, convolutional neural networks (CNNs) have demonstrated state-of-the-art performance in ocean remote sensing applications, owing to their hierarchical feature extraction capabilities and adaptable architectures (Wang and Li, 2024). However, deep learning models usually require substantial computational resources and long training time. Moreover, they encounter a complete retraining process if the structure is not sufficient to model the system, which limits their practicality in dynamic environments requiring frequent updates.

To address the demand for lightweight computation and efficient model updating, Chen and Liu (2018) proposed the broad learning system (BLS), which is based on the random vector functional-link neural network (RVFLNN). BLS adopts a flat network structure comprising feature nodes and enhancement nodes, which facilitates rapid learning and mitigates the vanishing gradient problem commonly observed in deep architectures. It has achieved recognition and regression performance comparable to conventional deep learning methods, while offering significantly improved training efficiency (Han et al., 2018; Yang et al., 2018; Zhang et al., 2018). Moreover, a notable advantage of BLS is its capacity for incremental learning, enabling the model to be updated with newly added samples or additional hidden nodes without requiring complete retraining. Owing to its efficient learning capability and flexible structure, BLS has been widely applied in various domains, including image processing and computer vision, medical and biomedical data analysis, control engineering, fault detection, system modeling, and prediction (Chu et al., 2025). Its structural adaptability also makes BLS particularly suitable for remote sensing applications, where continuous data acquisition necessitates frequent and efficient model updates (Wang et al., 2023).

It should be noted that while BLS achieves promising results on relatively simple benchmark datasets such as MNIST and NORB, its classification performance declines significantly on more complex datasets like SVHN, CIFAR-10, and CIFAR-100 (Liu et al., 2017b). Many studies have proposed hybrid models that integrate high-level feature extraction into the BLS framework to better handle complex image data. For example, Ma et al. (2022) proposed a multiscale random convolution BLS, which employs an adaptive weighted mean filter as the convolution kernel to extract local spatial features in the first layer for hyperspectral image classification. Hu et al. (2022) incorporated an attention mechanism into a variational expectation-maximization BLS model, markedly enhancing its capability in handling time-series data. Similarly, Yu and Zhao (2020) introduced a broad convolutional neural network (BCNN) for industrial fault diagnosis, using convolutional operations to capture nonlinear structural information and improve diagnostic accuracy. Zhang and Yuen (2021) proposed a fusion feature-based BLS (FF-BLS) that integrates a fixed-weight convolutional module to

extract fused image features, achieving competitive performance in crack detection tasks. Collectively, these studies highlight that incorporating high-dimensional feature extraction into the BLS architecture can effectively mitigate its limitations in complex image analysis while preserving its inherent computational efficiency. At present, the application of BLS in the field of ocean remote sensing remains relatively limited. As an efficient learning model, its potential in ocean remote sensing has yet to be fully explored.

To overcome the challenges of time-consuming training and limited update capability of deep learning models in large-scale, time-varying remote sensing datasets, this study proposes a fusion framework named Residual-Enhanced Broad Learning System (RE-BLS). The model integrates a residual module with a basic BLS to effectively harness the complementary strengths of both components. Specifically, the residual module leverages ResNet-50 to extract discriminative deep features from SAR images, while the BLS enables fast and efficient classification through its lightweight architecture. Benefiting from the combined strengths of residual learning and BLS, RE-BLS achieves classification accuracy comparable to that of conventional deep learning models, while significantly reducing training costs and preserving the incremental learning capability. These advantages make RE-BLS a promising solution for large-scale, dynamically evolving remote sensing applications.

The remainder of this paper is organized as follows. Section 2 provides a detailed description of the dataset employed in this study. The architecture of the proposed RE-BLS framework is introduced in Section 3. Section 4 presents the results and analysis. Discussions and conclusions are given in Sections 5 and 6, respectively.

2 DATASET

The TenGeoP-SARwv dataset provided by IFREMER comprises over 37 000 VV-polarized SAR images acquired by Sentinel-1A in wave mode (WV), with a spatial resolution of 50 m. It includes ten representative and expert-labeled geophysical phenomena frequently observed over the open ocean: pure ocean waves, wind streaks, micro convective cells, rain cells, biological slicks, sea ice, icebergs, low wind area, atmospheric fronts, and oceanic fronts (Wang et al., 2019). Each image depicts a single and distinct geophysical phenomenon characterized by clear features.

Figure 1 presents the representative SAR image samples for the ten geophysical phenomena. Each class exhibits distinct structural and textural characteristics, although certain similarities can also be observed across classes. For example, pure ocean waves appear as regularly distributed short wavelets with uniform texture, whereas wind streaks manifest as periodic linear patterns with relatively longer wavelengths. Micro convective cells exhibit periodic cellular structures, while rain cells are characterized by circular or semicircular bright/dark patches with irregular boundaries. Both atmospheric fronts and oceanic fronts exhibit elongated linear features. In addition, multiple phenomena may co-

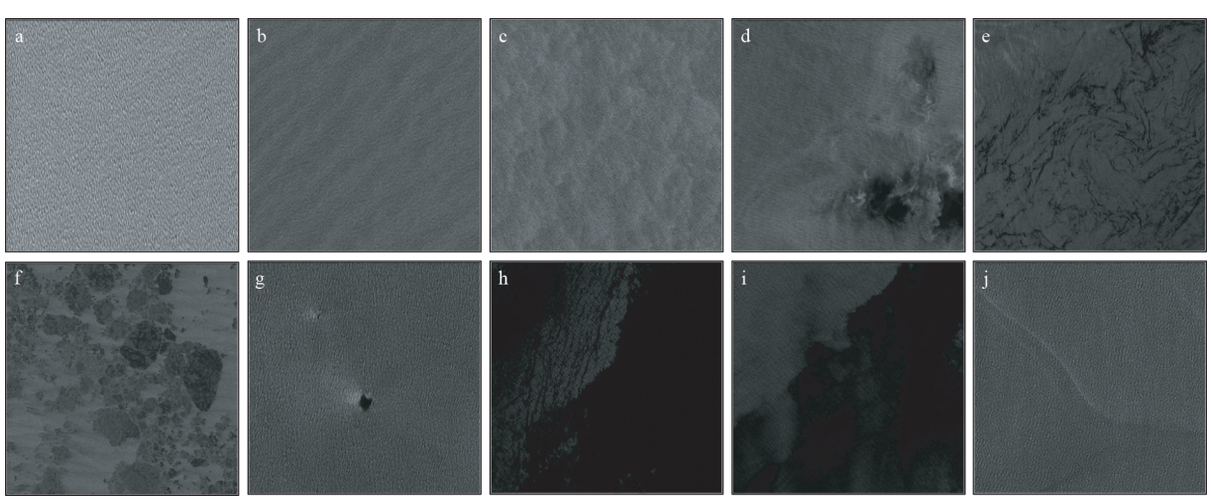


Fig.1 Example vignettes of ten geophysical phenomena

a. pure ocean waves; b. wind streaks; c. micro convective cells; d. rain cells; e. biological slicks; f. sea ice; g. icebergs; h. low wind area; i. atmospheric front; j. oceanic front.

occur. For instance, pure ocean waves frequently serve as the background in other classes, and low wind area samples are often dominated by extensive dark regions potentially accompanied by atmospheric front features.

In this study, GeoTIFF-formatted data were used for model training and evaluation. The dataset was randomly divided into 70% training set and 30% testing set. Among the ten classes, the number of samples in the iceberg, low wind area, and oceanic front classes was relatively limited. To address this class imbalance, a simple data augmentation strategy based on image rotation was applied to increase sample diversity without altering the inherent texture characteristics or grayscale distributions. Specifically, after the dataset was split, each image in the icebergs and low wind area categories was rotated 90° clockwise to double the number of samples. For the oceanic front class, each image was rotated both 90° clockwise and 90° counterclockwise, resulting in a threefold increase in sample size for this class. The final distribution of samples across ten categories is summarized in Table 1.

3 METHODOLOGY

3.1 Design of RE-BLS

The framework of the proposed RE-BLS model is illustrated in Fig.2. It consists of two main modules: a deep feature extraction module and a BLS classification module. The code for this study can be downloaded from the website: https://github.com/Oceanus-code. BLS is a shallow neural network architecture. It first applies a random projection to the input image matrix to generate an initial set of feature nodes, which are then expanded into enhancement nodes through nonlinear transformation. All feature and enhancement nodes are jointly connected to the output layer, where the output weights are computed using ridge regression. Moreover, benefiting from the dynamic stepwise updating mechanism of functional-link neural networks, BLS supports efficient incremental learning without requiring complete retraining. As illustrated in Fig.2, the model can be flexibly updated under three different scenarios, including the incremental enhancement nodes, mapping feature nodes, and new input data. Since the BLS model does not involve convolutional operations or gradient-based updates, it lacks the ability to automatically learn spatial structures from the input data. Consequently, its performance depends heavily on the discriminability and stability of the input features. In the case of SAR imagery, which often contains large homogeneous ocean surface regions, the random mapping process tends to treat these visually uniform areas indiscriminately, resulting in excessive feature redundancy and ultimately degrading classification performance.

Table 1 Detailed information of the training and testing dataset

Class	Training image	Testing image	Total image
Pure ocean waves (A0)	3 430	1 470	4 900
Wind streaks (A1)	3 357	1 440	4 797
Micro convective cells (A2)	3 218	1 380	4 598
Rain cells (A3)	3 318	1 422	4 740
Biological slicks (A4)	3 296	1 413	4 709
Sea ice (A5)	3 059	1 311	4 370
Icebergs (A6)	2 772	1 188	3 960
Low wind area (A7)	3 024	1 296	4 320
Atmospheric front (A8)	2 870	1 230	4 100
Oceanic front (A9)	2 517	1 080	3 597

CNNs have demonstrated remarkable capability in extracting multi-scale spatial features and have been widely applied in various image analysis tasks. Typically, CNNs are constructed by sequentially stacking multiple convolutional layers to form a hierarchical structure. However, as the network depth increases, conventional CNNs often suffer from the performance degradation problem. This phenomenon primarily stems from the degradation of information as it propagates through deeper layers. To address these issues, the residual network proposed by He et al. (2016) introduces shortcut connections within residual blocks. The skip connection mechanism introduced in ResNet significantly enhances the propagation of features across network layers. In each residual block, the input is not only processed through two convolutional layers to extract high-level semantic features but is also directly added to the output of the convolutional layers and passed to subsequent layers. This structure enables the effective fusion of shallow and deep features, allowing the network to preserve both abstract semantic information and low-level details such as edges and textures. For SAR images, which often contain oceanic phenomena characterized by weak textures and indistinct boundaries, this multi-level feature fusion is

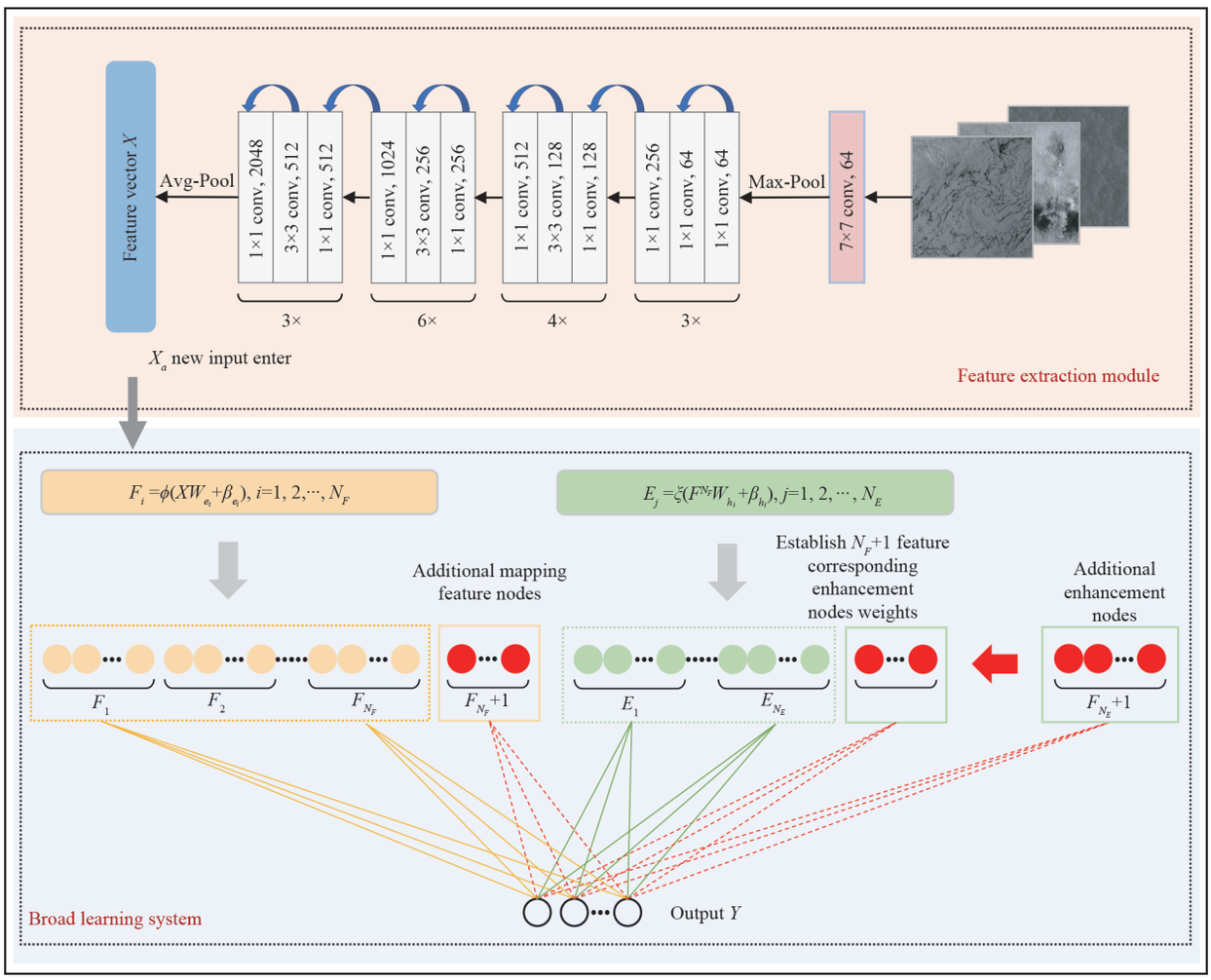


Fig.2 Architecture of Residual-Enhanced Broad Learning System

particularly beneficial in capturing sparse yet highly discriminative local regions.

We employed Gradient-weighted Class Activation Mapping (Grad-CAM) to visualize the role of ResNet-50 in extracting discriminative features from SAR imagery. Figure 3 presents several representative test samples, including the original SAR images and their corresponding saliency heatmaps. As illustrated, SAR images contain large homogeneous regions and limited texture information. Despite these challenges, ResNet-50 is able to accurately focus on critical areas such as frontal zones and the edges of rain cells. It effectively captures localized discriminative features that are essential for accurate classification. In summary, BLS offers a simple architecture with high computational efficiency, making it suitable for rapid processing of large-scale remote sensing data, but it lacks the ability to learn spatial structural features from complex SAR data. In contrast, CNNs provide strong feature extraction capabilities but are computationally expensive and less flexible for model updates. To combine their complementary strengths, this study proposes RE-BLS, which uses CNNs to enhance feature representation while preserving the training efficiency and incremental learning ability of BLS.

3.2 Feature extraction

In this study, ResNet-50 is adopted as the feature extraction module. To comprehensively assess the performance of different CNN models in classifying oceanic phenomena, we compared five widely used models, ResNet-50 (He et al., 2016), ResNet-18 (He et al., 2016), InceptionV3 (Szegedy et al., 2015), VGG16 (Simonyan and Zisserman, 2015), and MobileNetV3 (Howard et al., 2019), using the TenGeoP-SARwv dataset. The comparison focused on classification accuracy and training time. All experiments were conducted on the same training

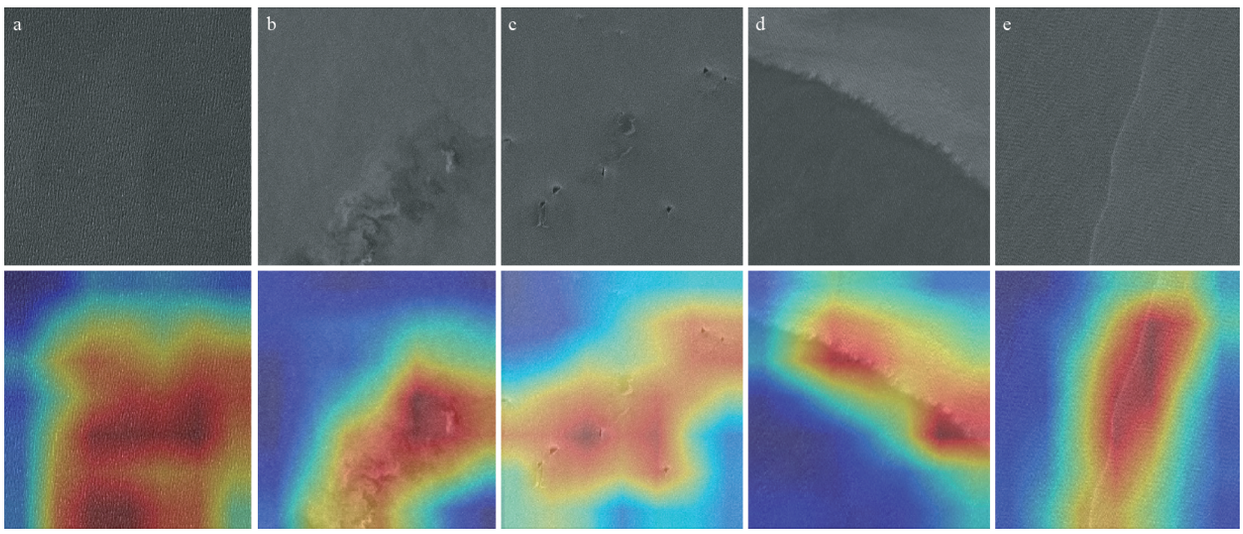


Fig.3 Original SAR images (top) and corresponding saliency maps (bottom) overlaid on SAR images for 5 different cases

Red: high value; blue: low value.

and testing datasets, and computations were performed on an identical hardware platform (NVIDIA GeForce RTX 4070 Ti). The training parameters were set as follows: a learning rate of 10^{-3}, a batch size of 64, and 50 epochs. To ensure a fair comparison, all networks were initialized with random weights. As shown in Fig.4, ResNet-50 achieved a testing accuracy of 97.33%, which was marginally lower than the 98.20% obtained by InceptionV3. However, it reduced training time by approximately 20% compared to the latter. These results indicate that both ResNet-50 and InceptionV3 are suitable for image feature extraction in this study. ResNet-50 was ultimately selected in this study.

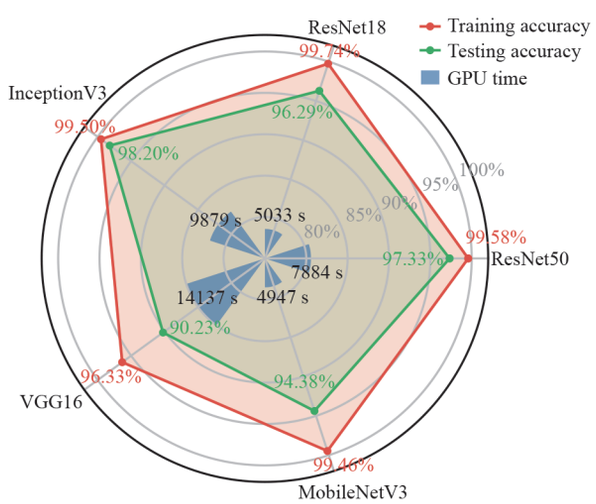


Fig.4 Comparison of classification accuracy and running time of different deep learning models

In addition, Table 2 summarizes the classification accuracy of the five models across the ten classes. As shown in Table 2, while InceptionV3 achieved the highest overall accuracy, followed closely by ResNet-50, both models exhibited reduced accuracy on the atmospheric front and oceanic front classes. These two categories display visually similar linear textures, which pose challenges for reliable discrimination. This highlights the inherent difficulty of distinguishing oceanic and atmospheric phenomena with complex and overlapping visual characteristics, especially when class boundaries are ambiguous and discriminative regions are limited.

3.3 Prototype BLS

3.3.1 Basic BLS

The BLS architecture comprises an input layer, a

Table 2 Classification accuracy (%) of different CNN models for ten geophysical categories

Method	A0	A1	A2	A3	A4	A5	A6	A7	A8	A9
Resnet-50	99.86	97.78	98.77	98.52	94.27	97.33	99.07	96.30	94.88	96.02
Resnet-18	99.93	98.12	94.20	95.99	96.32	93.97	98.91	94.44	95.69	94.72
Inception-V3	100	99.51	98.48	98.59	98.23	96.19	98.28	99.07	95.93	96.39
VGG-16	98.71	90.49	86.52	92.33	87.05	82.30	96.04	97.30	88.13	81.67
MobileNet-V3	100	99.72	83.33	96.48	94.69	93.36	98.91	85.80	93.41	98.24

node layer, and an output layer. The node layer comprises two types of nodes: mapping feature nodes and enhancement nodes. The feature vector extracted from the input image is denoted as $X \in \mathbb{R}^{N\times M}$, and the corresponding output is denoted as $Y \in \mathbb{R}^{N\times d}$, where d=10 in our classification task. Assume that there are N_F mapping feature nodes and each one can be formed as

$$F_i = \phi\left(XW_{e_i} + \beta_{e_i}\right),\ i = 1,\ 2,\ \cdots,\ N_F, \tag{1}$$

where W_{e_i} and β_{e_i} are randomly initialized weights and biases, respectively. All mapping feature nodes are concatenated into a matrix

$$F^{N_F} = \left[F_1,\ F_2,\ \cdots,\ F_{N_F}\right]. \tag{2}$$

Based on F^{N_F}, the enhancement nodes can be computed as

$$E_j = \xi\left(F^{N_F}W_{h_j} + \beta_{h_j}\right),\ j = 1,\ 2,\ \cdots,\ N_E, \tag{3}$$

where W_{h_j} and β_{h_j} are randomly generated. Combining all mapping feature nodes and enhancement nodes forms the final feature layer A. The final output of the BLS can be expressed as

$$Y = AW, \tag{4}$$

where the output weights W are computed using ridge regression approximation.

3.3.2 Incremental BLS

If the trained model fails to meet the desired performance requirements, BLS can dynamically increase its learning capacity by adding enhancement nodes or mapping feature nodes. Suppose the initial network consists of N_F mapping feature nodes and N_E enhancement nodes. When a new enhancement node E_{N_E+1} is added, it is computed as

$$E_{N_E+1} = \xi\left(F^{N_F}W_{h_{N_E+1}} + \beta_{h_{N_E+1}}\right). \tag{5}$$

Similarly, assume that the $(N_F+1)^{\text{th}}$ mapping feature node is added and denoted by

$$F_{N_F+1} = \phi\left(XW_{e_{N_F+1}} + \beta_{e_{N_F+1}}\right). \tag{6}$$

The corresponding enhancement nodes based on F_{N_F+1} are computed as

$$E_{F_{N_F+1}} = \left[\xi\left(F_{N_F+1}W_{hx_1} + \beta_{hx_1}\right), \cdots, \xi\left(F_{N_F+1}W_{hx_{N_E}} + \beta_{hx_{N_E}}\right)\right]. \tag{7}$$

After adding these new enhancement and mapping feature nodes, the updated node matrix becomes

$$A_{N_F+1}^{N_E+1} = \left[A|E_{N_E+1}|F_{N_F+1}|E_{F_{N_F+1}}\right]. \tag{8}$$

The pseudoinverse matrix could be computed as

$$(A_{N_F+1}^{N_E+1})^+ = \begin{bmatrix} A^+ - DB^T \\ B^T \end{bmatrix}, \tag{9}$$

where

$$D = A^+[E_{N_E+1}|F_{N_F+1}|E_{F_{N_F+1}}],$$

$$B^T = \begin{cases} (C)^+ & \text{if } C \neq 0 \\ (1 + D^TD)^{-1}D^T(A)^+ & \text{if } C = 0 \end{cases}$$

and $C = [E_{N_E+1}|F_{N_F+1}|E_{F_{N_F+1}}] - AD$.

Finally, the output weights are updated to incorporate the newly added nodes as follows

$$W_{N_F+1}^{N_E+1} = \begin{bmatrix} W - DB^TY \\ B^TY \end{bmatrix}. \tag{10}$$

It can be observed from the above equations that the updated output weight matrix incorporates both the original weights and the contributions from the newly added nodes.

In actual applications, datasets are frequently updated with new samples. Instead of retraining the entire model from scratch, BLS supports the efficient integration of newly added data through the incremental learning. For the new inputs X_a, the corresponding mapping feature nodes and enhancement nodes are computed as

$$F_{X_a}^{N_F} = \left[\phi\left(X_aW_{e_i} + \beta_{e_i}\right), \cdots, \phi\left(X_aW_{e_{N_F}} + \beta_{e_{N_F}}\right)\right], \tag{11}$$

$$E_{X_a}^{N_E} = \left[\xi\left(X_aW_{h_i} + \beta_{h_i}\right), \cdots, \zeta\left(X_aW_{h_{N_E}} + \beta_{h_{N_E}}\right)\right]. \tag{12}$$

The updated nodes matrix is denoted as $A_{X_a} = \left[F_{X_a}^{N_F}|E_{X_a}^{N_E}\right]$ and the augmented matrix becomes

$${}^{X_a}A = \begin{bmatrix} A \\ A_{X_a}^T \end{bmatrix}. \tag{13}$$

The associated pseudoinverse of ${}^{X_a}A$ can be efficiently computed as

$$\left({}^{X_a}A\right)^+ = \left[(A)^+ - BD^T|B\right], \tag{14}$$

where

$$D^T = A_{X_a}^T(A)^+,$$

$$B^T = \begin{cases} (C)^+ & \text{if } C \neq 0 \\ (1 + D^TD)^{-1}(A)^+D^T & \text{if } C = 0 \end{cases}$$

and $C=A_{X_a}^T-D^TA$.

Finally, the updated output weights are computed as

$$^{X_a}W=W+\left(Y_a^T-A_{X_a}^TW\right)B, \tag{15}$$

where Y_a is the label matrix corresponding to the new input samples X_a.

4 MODEL TRAINING AND TESTING

4.1 Hyperparameter optimization strategy

The proposed RE-BLS model involves three critical hyperparameters: the number of mapping feature windows N_1, the number of nodes in each mapping feature window N_2, and the number of enhancement nodes N_3. Proper selection of these parameters is essential for achieving optimal model performance. In the BLS module, the input data are linearly mapped to generate feature nodes, with N_1 and N_2 jointly determining the dimensionality of the initial feature representation. Excessively large values of N_1 or N_2 may lead to redundancy and overfitting. In contrast, the number of enhancement nodes N_3, which are generated through nonlinear transformations, plays a critical role in determining the model's representational capacity and typically exerts a stronger influence on classification performance. Based on experimental observations, the number of feature nodes is typically set between a few dozen and a few hundred, while the number of enhancement nodes can range from several thousand to over ten thousand.

We conducted a hyperparameter sensitivity analysis, as illustrated in Fig.5. The figure presents the variation in testing accuracy with different values of N_3 under various combinations of N_1 and N_2. The results show that the model is relatively insensitive to N_1 and N_2. With N_3 fixed, the testing accuracy remains comparable across most configurations, except when N_1=10 and N_2=10, where the performance degrades noticeably. In contrast, the model exhibits greater sensitivity to N_3. As N_3 increases, the overall testing accuracy shows an upward trend and gradually stabilizes. However, slight fluctuations are also observed during this process, indicating that the accuracy does not increase monotonically with the growth of this hyperparameter. Based on the hyperparameter sensitivity analysis and relevant studies, the search ranges for N_1, N_2, and N_3 were set to [1, 30], [1, 30], and [1, 3 000], respectively. These ranges offer a balance between model performance, stability, and search efficiency.

Bayesian optimization was employed in this study to determine the model hyperparameters due to its effectiveness in identifying near-optimal solutions under limited search budgets. Compared to traditional hyperparameter tuning methods such as grid search and random search, Bayesian optimization offers higher efficiency and a more informed search strategy. Grid search exhaustively evaluates all possible hyperparameters combinations, resulting in exponentially increasing computational costs as the number of parameters grows. While random search is generally more efficient than grid search in high-dimensional spaces, its sampling is entirely independent of previous evaluations, limiting its ability to refine the search direction. In contrast, Bayesian optimization is a global optimization strategy based on probabilistic modeling. It incorporates prior knowledge and observed evaluations to iteratively update the posterior distribution of the objective function using Bayes' theorem. An acquisition function is then used to select the most promising hyperparameter configuration, thereby facilitating a more efficient and targeted search process (Wu et al., 2019). In this study, the optimal hyperparameters for RE-BLS were determined to be N_1=28, N_2=18, and N_3=2 700.

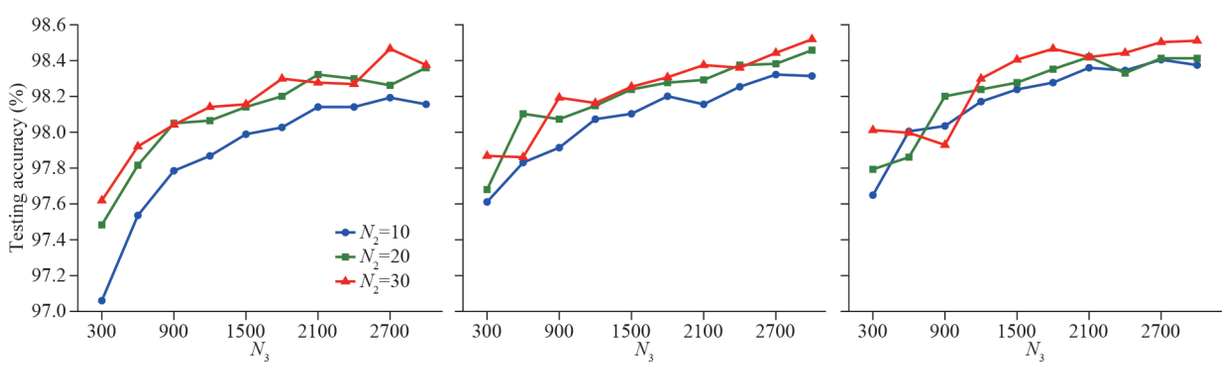


Fig.5 Testing accuracy of RE-BLS under different hyperparameter combinations

Left: N_1=10; middle: N_1=20; right: N_1=30.

4.2 RE-BLS model assessment

All training tasks were performed on a computer equipped with an NVIDIA GeForce RTX 4070 Ti GPU, consistent with the hardware configuration described in Section 3. The training and testing results of RE-BLS are presented in Table 3. As shown in Table 3, the proposed RE-BLS model achieves a training accuracy of 99.09% and a testing accuracy of 98.48%, demonstrating performance comparable to ResNet-50. In terms of computational efficiency, RE-BLS exhibits a clear advantage. Under the same GPU settings, ResNet-50 requires 7 884.26 s for training, whereas RE-BLS completes the process in only 151.37 s, corresponding to an approximately 51-fold reduction in running time. It is worth noting that most of the computational cost of RE-BLS comes from the feature extraction stage using the pretrained ResNet-50, while the BLS training itself requires only about 5 s.

To evaluate the contribution of the feature extraction module in the proposed framework, a comparative experiment was conducted using the original BLS model without the deep feature extraction module. Given the limited capacity of BLS for handling complex images, the hyperparameter search space was expanded accordingly, with N_1 and N_2 set within the range [1, 200], and N_3 within [1, 10 000]. The optimal hyperparameters for the BLS model were determined to be N_1=2, N_2=36, and N_3= 8 300. As shown in Table 3, the training and testing accuracies of the original BLS model are only 63.10% and 56.07%, respectively, which are substantially lower than those obtained by the RE-BLS. These results indicate that the standalone BLS model struggles to handle complex image data, which severely degrades its classification performance. In contrast, the integration of ResNet-50 strengthens the model's representational capacity and achieves a notable improvement in accuracy. This comparison clearly confirms the necessity of incorporating a deep feature extraction module into the RE-BLS framework. In summary, the results discussed above demonstrate that the proposed RE-BLS framework, by integrating feature extraction modules into the BLS architecture, achieves excellent performance in ocean phenomenon classification tasks, with notable improvements in both classification accuracy and efficiency.

4.3 Error analysis

Despite the strong overall classification performance of RE-BLS, some misclassifications were still observed. To further assess the model's performance across all categories, a normalized confusion matrix is presented in Fig.6. In the matrix, rows denote the ground-truth classes and columns represent the predicted classes produced by RE-BLS. Most classes achieved classification accuracies exceeding 0.98. However, the performance for the atmospheric fronts and oceanic fronts was relatively lower. In particular, the atmospheric front class was frequently confused with the low wind area class. Additionally, approximately 4% of oceanic front samples were misclassified as atmospheric front.

A comprehensive review of all misclassified samples in the RE-BLS test set was conducted, and the corresponding predicted class probabilities from the Softmax output were extracted. Figure 7 presents four representative examples, including three cases where oceanic front images were misclassified as atmospheric front, and one case where an atmospheric front image was misclassified

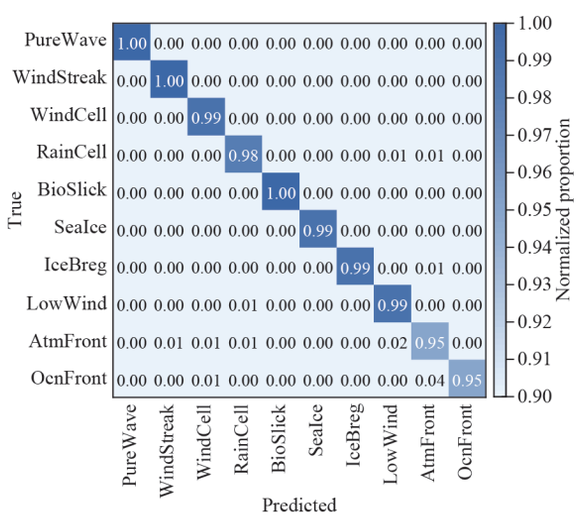


Fig.6 The normalized confusion matrix of RE-BLS model

Table 3 Comparison of classification performance among BLS, RE-BLS, and ResNet-50

Method	Number of nodes	Training accuracy (%)	Testing accuracy (%)	Running time (s)
BLS	(2, 36, 8 300)	63.10	56.07	89.85
RE-BLS	(28, 18, 2 700)	99.09	98.48	151.37
ResNet-50	–	99.58	97.33	7 884.26

– indicates that ResNet-50 does not use the node configuration adopted in BLS and RE-BLS.

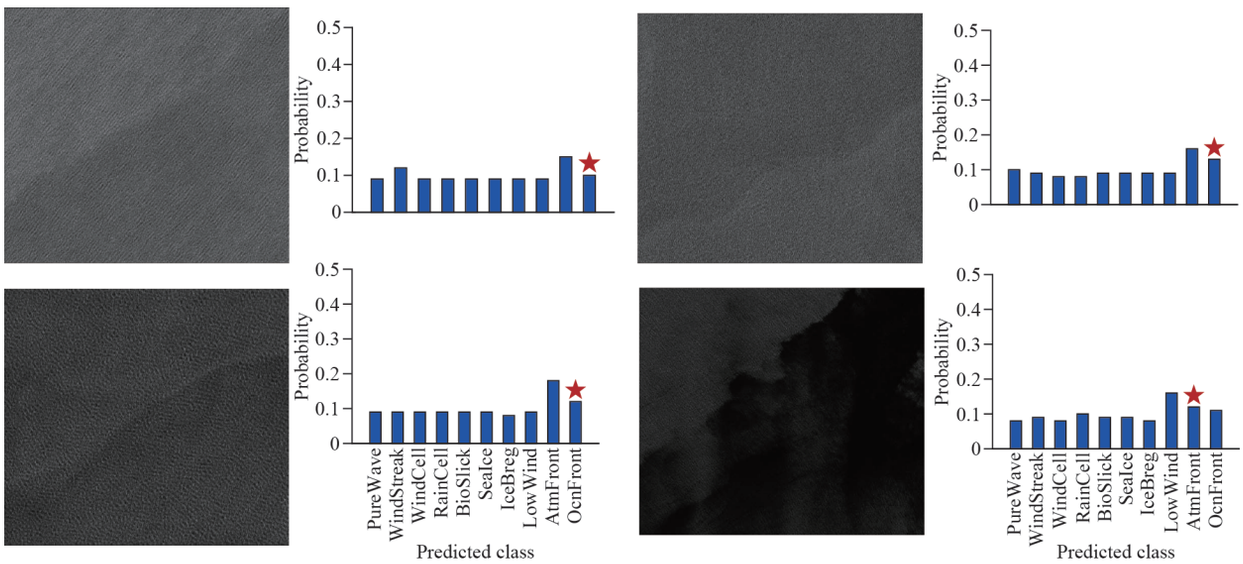


Fig.7 Misclassified examples from RE-BLS along with the predicted class probabilities across all categories

The red star indicates the ground-truth class for each SAR image.

as a low wind area. Most misclassifications arise from image samples in which the oceanic phenomena are weakly expressed or visually ambiguous. Identifying oceanic fronts typically relies on the presence of fine bright-line structures in SAR imagery, which reflect radar backscatter gradients associated with frontal boundaries. However, in many misclassified samples, these features appear blurred or poorly defined, leading to weaker frontal signatures compared to those observed in correctly classified samples. Likewise, the atmospheric front image that was misclassified as a low wind area contains extensive dark gray to black regions, closely resembling the characteristic "dark patch" patterns commonly observed in low wind scenes. This visual similarity likely led to the model's misclassification. These examples indicate that the primary cause of misclassification stems from the high degree of visual similarity among different image classes. This similarity manifests in two principal aspects. First, SAR images across different categories often exhibit similar grayscale distributions. The target phenomena frequently lack distinctive brightness or contrast cues, making effective discrimination challenging. Second, the target classes exhibit notable similarities in morphological structure and spatial scale. For instance, certain oceanic fronts and atmospheric fronts both appear as elongated linear features with specific orientations and comparable spatial extents, making them difficult to distinguish.

4.4 Incremental learning of RE-BLS

4.4.1 Increment of nodes

Incremental learning is one of the key advantages of the BLS. In conventional deep learning models, performance improvement typically requires increasing network depth, tuning hyperparameters, or expanding the training dataset. These adjustments often necessitate architectural reconfiguration and extensive retraining, leading to substantial computational costs. In contrast, BLS adopts a dynamically expandable architecture that supports efficient model adaptation through the incremental addition of enhancement nodes, mapping feature nodes, or new input samples, without the need to retrain the entire network.

To validate the feasibility of updating and optimizing the RE-BLS model through incremental node expansion, two incremental learning schemes were designed based on the optimal hyperparameters (28×18×2 700): (1) adding enhancement nodes only, and (2) simultaneously increasing both feature nodes and enhancement nodes. In the first scheme, the initial network was configured with 144 (8×18) feature nodes and 300 enhancement nodes. During incremental learning, 600 enhancement nodes were added at each step across five steps, resulting in a final network structure of (8×18×3 300). In the second scheme, starting from the same initial network, both feature and enhancement nodes were incrementally added. Specifically, 90 feature nodes and 600 enhancement nodes were added at each

step, also over five incremental steps.

The performance of the RE-BLS model under incremental learning is presented in Fig.8a, with detailed results provided in Table 4. When only enhancement nodes were incrementally added, the initial testing accuracy was 97.31%. While a slight improvement was observed during the early stages, accuracy began to decline after the fourth increment. This trend suggests that although adding enhancement nodes can initially enhance performance, excessive growth may introduce redundant features that ultimately degrade classification accuracy. In contrast, when both feature and enhancement nodes were jointly increased, the testing accuracy steadily improved, reaching 98.25% as the network expanded. Notably, after the fourth increment, the node configuration approached its optimal structure, yielding a testing accuracy of 98.21%, which was slightly lower than the 98.48% achieved by one-time training with optimal hyperparameters. This discrepancy may be attributed to constraints in parameter updates during incremental learning, which can hinder the model from fully converging to its optimal state. Overall, the results indicate that simultaneous expansion of feature and enhancement nodes is more effective for improving classification

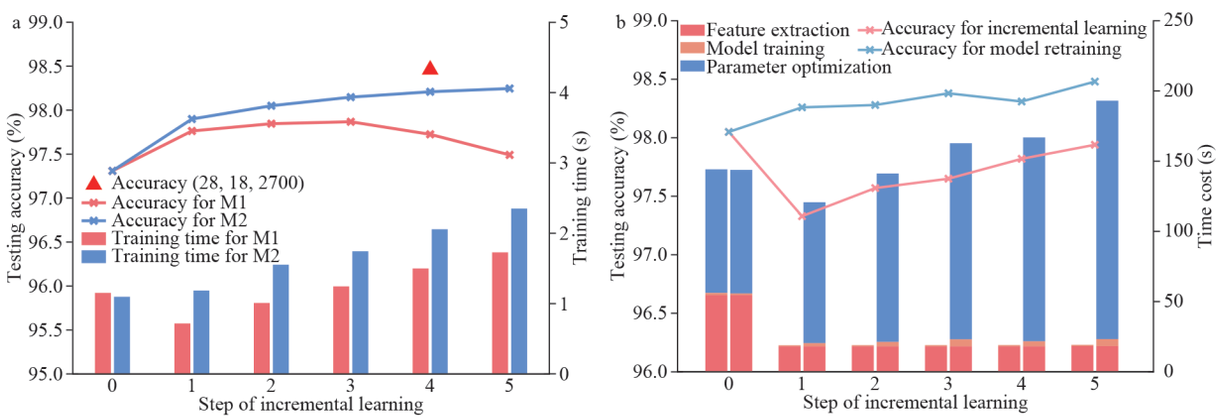


Fig.8 Performance comparison of RE-BLS under different incremental learning strategies

a. classification accuracy and training time for two node-based incremental learning strategies; b. classification accuracy and training time for data incremental learning and model retraining.

Table 4 Training and testing results for incremental learning

Step	N_F	N_E	Training accuracy (%)	Testing accuracy (%)	Time cost (s)		
					Feature extraction	Model training	Accumulative time
(M1): increment of enhancement nodes							
0	144	300	97.67	97.31	139.00	1.15	140.15
1	144	900	98.19	97.76	–	0.72	140.87
2	144	1 500	98.50	97.85	–	1.01	141.88
3	144	2 100	98.60	97.87	–	1.24	143.12
4	144	2 700	98.61	97.73	–	1.50	144.62
5	144	3 300	98.53	97.49	–	1.73	146.35
(M2): increment of feature and enhancement nodes							
0	144	300	97.67	97.31	139.00	1.10	140.10
1	234	900	98.38	97.90	–	1.19	141.29
2	324	1 500	98.67	98.05	–	1.55	142.84
3	414	2 100	98.90	98.15	–	1.74	144.58
4	504	2 700	99.11	98.21	–	2.06	146.64
5	594	3 300	99.26	98.25	–	2.35	148.99

– indicates that no additional feature extraction is required in the subsequent incremental learning steps.

accuracy and maintaining training stability in incremental learning scenarios.

In terms of training efficiency, the inherent computational advantages of the BLS model, combined with the incremental learning mechanism, ensure that the cumulative training time increases only marginally even after six complete training rounds. This is primarily because the feature extraction stage dominates the overall computation load, typically consuming around 90% of total runtime. In contrast, the increase in BLS training time across updates is minimal and has a negligible impact on overall performance. As a result, the overall training process remains highly efficient, even after multiple rounds of incremental updates.

4.4.2 Increment of inputs

In remote sensing applications, the continuous accumulation of acquired data imposes increasing demands on the efficiency of model updating. The proposed RE-BLS is well suited for modeling high-volume, time-varying systems. It incrementally integrates new training samples while preserving previously learned knowledge, thereby avoiding redundant retraining. We also evaluated the input-based incremental learning capability of RE-BLS for ocean SAR image classification, and the experimental procedure is as follows:

1) Define the global dataset as the full set of samples. Construct the initial training set by randomly selecting 3/8 of the samples from each class, while retaining the same testing set described in Section 2.

2) Apply Bayesian optimization to the initial training set to obtain the optimal hyperparameters, which were determined as (27, 11, 1 900).

3) Starting from the initial training set, perform five incremental learning stages by randomly adding 1/8 of the data from each class at each stage. The hyperparameters remain fixed throughout all incremental updates.

Table 5 summarizes the training and testing performance of RE-BLS throughout the data incremental learning process and model retraining. The initial testing accuracy was 98.05%, which temporarily declined to 97.33% after the first incremental update. This performance drop may be attributed to catastrophic forgetting, a phenomenon in which previously acquired knowledge is partially lost as the model adapts to new data (Liu et al., 2017b). To mitigate this issue, future extensions of RE-BLS could incorporate regularization strategies to constrain parameter changes, or employ a small replay buffer to retain representative samples from previous tasks, thereby preserving prior knowledge during incremental learning. As incremental learning progressed, the testing accuracy of RE-BLS

Table 5 Training and testing results for data incremental learning and model retraining of RE-BLS

Step	Input sample	Node	Training accuracy (%)	Testing accuracy (%)	Time cost (s)			
					Parameter optimization	Feature extraction	Model training	Total
(M3): data incremental learning								
0	11 559	(27, 11, 1 900)	99.40	98.05	87.92	54.61	1.65	144.18
1	11 559→15 412	(27, 11, 1 900)	98.75	97.33	–	18.20	0.67	18.87
2	15 412→19 265	(27, 11, 1 900)	98.70	97.57	–	18.20	0.73	18.93
3	19 265→23 118	(27, 11, 1 900)	98.62	97.65	–	18.20	0.76	18.96
4	23 118→26 971	(27, 11, 1 900)	98.61	97.82	–	18.20	0.79	18.99
5	26 971→30 861	(27, 11, 1 900)	98.52	97.94	–	18.36	0.83	19.19
(M4): model retraining								
0	11 559	(27, 11, 1 900)	99.40	98.05	87.92	54.61	1.25	143.78
1	11 559→15 412	(26, 23, 1 800)	99.24	98.26	100.29	18.20	2.26	120.75
2	15 412→19 265	(23, 13, 3 000)	99.30	98.28	119.86	18.20	3.15	141.21
3	19 265→23 118	(29, 25, 2 900)	99.34	98.38	139.56	18.20	5.00	162.76
4	23 118→26 971	(28, 13, 2 500)	99.06	98.31	145.09	18.20	3.59	166.88
5	26 971→30 861	(28, 18, 2 700)	99.09	98.48	169.71	18.36	4.97	193.04

– indicates that parameter optimization is performed only at Step 0.

gradually improved from 97.33% to 97.94%, indicating that the model was able to effectively leverage newly introduced data to enhance its performance. Nevertheless, the final testing accuracy of 97.94% remained slightly lower than the initial performance. For comparison, one-shot training using the entire dataset of 30 861 samples achieved a higher testing accuracy of 98.48%, outperforming the incremental approach. During one-shot training, the model extracts feature from the entire dataset at once, enabling the generation of more globally representative feature nodes. In contrast, RE-BLS conducts incremental training using a fixed network structure defined by the initial dataset, incorporating only newly added samples at each stage. This constraint limits the model's ability to construct a holistic and expressive feature space.

The total computational cost of the RE-BLS incremental learning process comprises three main components: hyperparameter optimization, feature extraction, and model training. As shown in Table 5, hyperparameter optimization and feature extraction account for the majority of the computation time, whereas model training requires only a few seconds. During the initial training phase, the total runtime was 144.18 s, including 87.92 s for hyperparameter optimization, 54.61 s for feature extraction, and only 1.65 s for model training. In subsequent incremental phases, since the hyperparameters remain fixed, the computational cost is primarily driven by feature extraction and BLS model updates. Each incremental round requires approximately 19 s. After multiple rounds of incremental updates, the overall computational time remains relatively stable and comparable to that of one-shot training.

As an alternative to incremental learning, the RE-BLS model can be retrained at each stage. In this scheme, the optimal hyperparameters are re-optimized, and the model is retrained using a combined dataset of previously seen and newly added samples. Compared to incremental learning, the retrained model consistently achieves higher classification accuracy as the dataset grows. By re-tuning hyperparameters and retraining the model as new data is introduced, RE-BLS adapts more effectively to distributional shifts, leading to improved feature representation and enhanced generalization performance. However, this performance gain comes at the expense of significantly increased computational costs. As the dataset expands, the time required for hyperparameter optimization and model training increases accordingly. The total training time grows from 120.75 to 193.04 s, which is substantially higher than the 19 s required per stage in the incremental learning approach. To further evaluate the stability of the incremental learning process, a preliminary stress test was conducted. For stress testing, a finer partition was adopted, in which the training data were divided into twenty subsets and sequentially introduced into the RE-BLS model. The results show that the testing accuracy improves rapidly in the early stages and gradually stabilizes without obvious performance degradation. However, a performance gap remains compared to full retraining, and the improvement becomes marginal after several incremental updates. This suggests that once the model performance reaches a convergence stage, retraining with the full dataset may be necessary to achieve optimal performance. It should be noted that this test simulates incremental updates by partitioning a limited dataset, which differs from real-world continuous data acquisition scenarios. Thus, it serves as a preliminary validation under constrained conditions, and future work will explore the model's stability in real-world operational environments.

For a brief summary, the two model update strategies offer distinct advantages. Incremental learning enables rapid model updates with minimal computational overhead. Although classification accuracy improves progressively with each update, it remains slightly lower than that achieved through full retraining. By contrast, retraining provides superior classification performance but incurs substantially higher computational costs. Therefore, incremental learning provides a practical trade-off between computational cost and classification accuracy. This makes incremental learning of RE-BLS a viable and efficient strategy for model adaptation in large-scale and evolving systems, such as those encountered in remote sensing scenarios characterized by continuous data growth and temporal variability.

5 DISCUSSION

This study proposes an ocean phenomenon recognition model, termed RE-BLS. Although it shows promising performance, several limitations remain. First, the model is trained and evaluated on a labeled SAR dataset derived from Sentinel-1 wave mode data, which has relatively consistent imaging conditions. When applied to other imaging modes, differences in spatial resolution, observation scale,

and imaging geometry may affect its performance, indicating that its generalization ability requires further validation. Second, the dataset is designed for single-label classification, where each image corresponds to one dominant geophysical phenomenon. Accordingly, RE-BLS is inherently a single-label classification model. However, different types of ocean phenomena often coexist within a single SAR image. The current model cannot predict multiple categories simultaneously, which limits its applicability in complex environments. Future work will explore multi-label learning or object detection frameworks to improve adaptability. In addition, incorporating attention mechanisms will be considered to enhance the model's ability to focus on subtle and spatially distributed features in more complex scenes. It should also be noted that, although the dataset was constructed through extensive screening of Sentinel-1 wave mode data and with reference to existing ocean SAR studies, some degree of uncertainty due to subjective labeling is unavoidable. This issue is particularly pronounced for atmospheric and oceanic fronts, which exhibit complex physical mechanisms and similar appearances in SAR imagery, making them difficult to distinguish. In some cases, features labeled as atmospheric fronts may actually be associated with sea surface temperature variations. Such label noise may affect model training and classification performance. To address this issue, future work will incorporate multi-source auxiliary data for independent validation, thereby improving data quality and enhancing the robustness of the model.

Currently, the BLS has been applied in various fields and is known for its high training efficiency and fast incremental updates. However, its application in remote sensing remains limited. With the rapid advancement of ocean remote sensing, the field has entered the era of big data. In practical applications, processing remote sensing data faces multiple challenges, including large data volumes, strict timeliness requirements, and limited computational resources. These constraints make lightweight models particularly attractive, as they enable preliminary processing and information extraction directly at the data acquisition stage, reducing data transmission load and improving system responsiveness (Li et al., 2021a; Zhang et al., 2022b; Leyva-Mayorga et al., 2023). Compared with complex deep learning models, which are often difficult to deploy in resource-constrained environments such as those on spaceborne, airborne, or other edge platforms, BLS is well suited to such scenarios. Its flat architecture controls parameter growth and reduces storage requirements, while its output weights can be efficiently computed via pseudoinverse, lowering computational cost. In addition, its incremental learning capability supports rapid model updates in dynamic environments. Overall, BLS provides an effective and practical solution for remote sensing applications.

6 CONCLUSION

This study proposed a Residual-Enhanced Broad Learning System, called RE-BLS, for multi-class ocean phenomena recognition with SAR imagery. By integrating a pre-trained ResNet-50 for deep feature extraction with the BLS as a lightweight classifier, the proposed model combines the representational strength of deep learning with the computational efficiency of broad learning.

Experimental results on the TenGeoP-SARwv dataset show that RE-BLS substantially outperforms the original BLS, increasing classification accuracy from 56.07% to 98.48%. This improvement underscores the critical importance of integrating deep feature extraction. Furthermore, compared to several classical deep learning models, RE-BLS achieves competitive classification performance while significantly reducing training time. For example, RE-BLS achieves an approximately 50-fold reduction in training time compared with a standalone ResNet-50 model, effectively balancing accuracy and computational efficiency. Additionally, RE-BLS exhibits strong incremental learning capabilities. When its performance is insufficient, applying data incremental learning and node incremental learning can lead to a performance improvement without full model retraining. This high efficiency is particularly advantageous in remote sensing applications, where data acquisition is continuous and large volumes of satellite observations are regularly generated. Overall, RE-BLS provides an efficient, flexible, and reliable solution for intelligent recognition and classification of ocean phenomena with high resolution SAR images, and holds strong potential for practical deployment in ocean monitoring and environmental surveillance tasks.

7 DATA AVAILABILITY STATEMENT

The TenGeoP-SARwv dataset used in this study is publicly available from the sea scientific open

data publication (SEANOE) repository and can be accessed at https://www.seanoe.org/data/00456/56796/.

8 ACKNOWLEDGMENT

The authors are grateful to IFREMER for providing the TenGeoP-SARwv dataset that is used in this study.

References

Bojinski S, Verstraete M, Peterson T C et al. 2014. The concept of essential climate variables in support of climate research, applications, and policy. *Bulletin of the American Meteorological Society*, **95**(9): 1431-1443, https://doi.org/10.1175/BAMS-D-13-00047.1.

Chen C L P, Liu Z L. 2018. Broad learning system: an effective and efficient incremental learning system without the need for deep architecture. *IEEE Transactions on Neural Networks and Learning Systems*, **29**(1): 10-24, https://doi.org/10.1109/TNNLS.2017.2716952.

Chu Y H, Guo Y L, Ding W P et al. 2025. Broad learning systems: an overview of recent advances, applications, challenges and future directions. *Neurocomputing*, **641**: 130337, https://doi.org/10.1016/j.neucom.2025.130337.

Duo Z J, Wang W K, Wang H Z. 2019. Oceanic mesoscale eddy detection method based on deep learning. *Remote Sensing*, **11**(16): 1921, https://doi.org/10.3390/rs11161921.

Han Y, Li T S, Zuo Y et al. 2018. Application of broad learning system for container number identification. *In*: International Conference on Security, Pattern Analysis, and Cybernetics (SPAC). IEEE, Jinan, China. p.332-336, https://doi.org/10.1109/SPAC46244.2018.8965520.

He J L, Wang Y H, Liu H W. 2021. Ship classification in medium-resolution SAR images via densely connected triplet CNNs integrating fisher discrimination regularized metric learning. *IEEE Transactions on Geoscience and Remote Sensing*, **59**(4): 3022-3039, https://doi.org/10.1109/TGRS.2020.3009284.

He K M, Zhang X Y, Ren S Q et al. 2016. Deep residual learning for image recognition. *In*: 2016 IEEE Conference on Computer Vision and Pattern Recognition (CVPR). IEEE, Las Vegas, USA. p.770-778, https://doi.org/10.1109/CVPR.2016.90.

Howard A, Sandler M, Chen B et al. 2019. Searching for MobileNetV3. *In*: Proceedings of the IEEE/CVF International Conference on Computer Vision. IEEE, Seoul, Korea (South). p. 1314-1324, https://doi.org/10.1109/ICCV.2019.00140.

Hu X, Wei X, Gao Y et al. 2022. Variational expectation maximization attention broad learning systems. *Information Sciences*, **608**: 597-612, https://doi.org/10.1016/j.ins.2022.06.074.

Huang B X, Ge L Y, Chen X Y et al. 2022. Vertical structure-based classification of oceanic eddy using 3-D convolutional neural network. *IEEE Transactions on Geoscience and Remote Sensing*, **60**: 4203614, https://doi.org/10.1109/TGRS.2021.3103251.

Huang Y, Ren Y B, Li X F. 2024. Deep learning techniques for enhanced sea-ice types classification in the Beaufort Sea via SAR imagery. *Remote Sensing of Environment*, **308**: 114204, https://doi.org/10.1016/j.rse.2024.114204.

Leyva-Mayorga I, Martinez-Gost M, Moretti M et al. 2023. Satellite edge computing for real-time and very-high resolution earth observation. *IEEE Transactions on Communications*, **71**(10): 6180-6194, https://doi.org/10.1109/TCOMM.2023.3296584.

Li F D, Liu Z Y, Shen W X et al. 2021a. A remote sensing and airborne edge-computing based detection system for pine wilt disease. *IEEE Access*, **9**: 66346-66360, https://doi.org/10.1109/ACCESS.2021.3073929.

Li X M, Sun Y, Zhang Q. 2021b. Extraction of sea ice cover by Sentinel-1 SAR based on support vector machine with unsupervised generation of training data. *IEEE Transactions on Geoscience and Remote Sensing*, **59**(4): 3040-3053, https://doi.org/10.1109/TGRS.2020.3007789.

Liu Y J, Qiu M, Liu C et al. 2017a. Big data challenges in ocean observation: a survey. *Personal and Ubiquitous Computing*, **21**(1): 55-65, https://doi.org/10.1007/s00779-016-0980-2.

Liu Z L, Zhou J, Chen C L P. 2017b. Broad learning system: feature extraction based on K-means clustering algorithm. *In*: 2017 4th International Conference on Information, Cybernetics and Computational Social Systems (ICCSS). IEEE, Dalian, China. p.683-687, https://doi.org/10.1109/ICCSS.2017.8091501.

Ma Y, Liu Z, Chen C L P. 2022. Multiscale random convolution broad learning system for hyperspectral image classification. *IEEE Geoscience and Remote Sensing Letters*, **19**: 5503605, https://doi.org/10.1109/LGRS.2021.3060876.

Rogers M S J, Fox M, Fleming A et al. 2024. Sea ice detection using concurrent multispectral and synthetic aperture radar imagery. *Remote Sensing of Environment*, **305**: 114073, https://doi.org/10.1016/j.rse.2024.114073.

Santana O J, Hernández-Sosa D, Smith R N. 2022. Oceanic mesoscale eddy detection and convolutional neural network complexity. *International Journal of Applied Earth Observation and Geoinformation*, **113**: 102973, https://doi.org/10.1016/j.jag.2022.102973.

Simonyan K, Zisserman A. 2015. Very deep convolutional networks for large-scale image recognition. *In*: 3rd International Conference on Learning Representations. Computational and Biological Learning Society, San Diego, USA. p.1-14, https://arxiv.org/abs/1409.1556.

Sun K, Chong J S, Diao L J et al. 2022. On the use of ocean surface Doppler velocity for oceanic front extraction from Chinese Gaofen-3 SAR data. *IEEE Journal of Selected Topics in Applied Earth Observations and Remote Sensing*, **15**: 2709-2720, https://doi.org/10.1109/JSTARS.2022.3162445.

Sun X, Zhang M, Dong J Y et al. 2021. A deep framework for eddy detection and tracking from satellite sea surface height data. *IEEE Transactions on Geoscience and Remote Sensing*, **59**(9): 7224-7234, https://doi.org/10.

1109/TGRS.2020.3032523.

Szegedy C, Liu W, Jia Y Q et al. 2015. Going deeper with convolutions. *In*: Proceedings of the IEEE Conference on Computer Vision and Pattern Recognition. IEEE, Boston, USA. p.1-9, https://doi.org/10.1109/CVPR.2015.7298594.

Temitope Yekeen S, Balogun A L, Wan Yusof K B. 2020. A novel deep learning instance segmentation model for automated marine oil spill detection. *ISPRS Journal of Photogrammetry and Remote Sensing*, **167**: 190-200, https://doi.org/10.1016/j.isprsjprs.2020.07.011.

Vasavi S, Divya C, Sarma A S. 2021. Detection of solitary ocean internal waves from SAR images by using U-Net and KDV solver technique. *Global Transitions Proceedings*, **2**(2): 145-151, https://doi.org/10.1016/j.gltp.2021.08.063.

Wang C, Mouche A, Tandeo P et al. 2019. A labelled ocean SAR imagery dataset of ten geophysical phenomena from Sentinel-1 wave mode. *Geoscience Data Journal*, **6**(2): 105-115, https://doi.org/10.1002/gdj3.73.

Wang H Y, Li X F. 2024. DeepBlue: advanced convolutional neural network applications for ocean remote sensing. *IEEE Geoscience and Remote Sensing Magazine*, **12**(1): 138-161, https://doi.org/10.1109/MGRS.2023.3343623.

Wang S, Yuen K V, Yang X F et al. 2023. Tropical cyclogenesis detection from remotely sensed sea surface winds using graphical and statistical features-based broad learning system. *IEEE Transactions on Geoscience and Remote Sensing*, **61**: 4203815, https://doi.org/10.1109/TGRS.2023.3266814.

Wu J, Chen X Y, Zhang H et al. 2019. Hyperparameter optimization for machine learning models based on Bayesian optimization. *Journal of Electronic Science and Technology*, **17**(1): 26-40, https://doi.org/10.11989/JEST.1674-862X.80904120.

Xu L L, Li J, Brenning A. 2014. A comparative study of different classification techniques for marine oil spill identification using RADARSAT-1 imagery. *Remote Sensing of Environment*, **141**: 14-23, https://doi.org/10.1016/j.rse.2013.10.012.

Xu X F, Du Y L, Cui G X et al. 2022. Ocean front detection from SAR imagery using SLIC superpixel segmentation method. *In*: IEEE International Geoscience and Remote Sensing Symposium (IGARSS). IEEE, Kuala Lumpur, Malaysia. p.2578-2581, https://doi.org/10.1109/IGARSS46834.2022.9884664.

Yang L, Song S J, Chen C L P. 2018. Transductive transfer learning based on broad learning system. *In*: IEEE International Conference on Systems, Man, and Cybernetics (SMC). IEEE, Miyazaki, Japan. p.912-917, https://doi.org/10.1109/SMC.2018.00162.

Yang X, Zhang X, Wang N N et al. 2022. A robust one-stage detector for multiscale ship detection with complex background in massive SAR images. *IEEE Transactions on Geoscience and Remote Sensing*, **60**: 5217712, https://doi.org/10.1109/TGRS.2021.3128060.

Yu W K, Zhao C H. 2020. Broad convolutional neural network based industrial process fault diagnosis with incremental learning capability. *IEEE Transactions on Industrial Electronics*, **67**(6): 5081-5091, https://doi.org/10.1109/TIE.2019.2931255.

Zhang T, Liu Z L, Wang X H et al. 2018. Facial expression recognition via broad learning system. *In*: IEEE International Conference on Systems, Man, and Cybernetics (SMC). IEEE, Miyazaki, Japan. p.1898-1902, https://doi.org/10.1109/SMC.2018.00328.

Zhang X D, Wang H Y, Wang S et al. 2022a. Oceanic internal wave amplitude retrieval from satellite images based on a data-driven transfer learning model. *Remote Sensing of Environment*, **272**: 112940, https://doi.org/10.1016/j.rse.2022.112940.

Zhang Y, Yuen K V. 2021. Crack detection using fusion features-based broad learning system and image processing. *Computer-Aided Civil and Infrastructure Engineering*, **36**(12): 1568-1584, https://doi.org/10.1111/mice.12753.

Zhang Z Q, Qu Z, Liu S Y et al. 2022b. Expandable on-board real-time edge computing architecture for Luojia3 intelligent remote sensing satellite. *Remote Sensing*, **14**(15): 3596, https://doi.org/10.3390/rs14153596.

Zi N N, Li X M, Gade M et al. 2024. Ocean eddy detection based on YOLO deep learning algorithm by synthetic aperture radar data. *Remote Sensing of Environment*, **307**: 114139, https://doi.org/10.1016/j.rse.2024.114139.